PCCP

PAPER

View Article Online
View Journal | View Issue

Cite this: *Phys. Chem. Chem. Phys.*, 2025, **27**, 25512

Energetics and kinetics of alkali ion exchange in analcime

Jinyi Liu, [a] An T. Ta, †[a] R. Seaton Ullberg, ‡[a] Jean Wilfried Hounfodji, [b] Michael Badawi, [b] Hans-Conrad zur Loye [c] and Simon R. Phillpot *[a]

Received 22nd June 2025,
Accepted 9th October 2025

DOI: 10.1039/d5cp02373d

rsc.li/pccp

We employ density functional theory calculations to investigate the energetics and diffusion mechanisms of alkali metal ions (Na^+, K^+, Rb^+, and Cs^+) within the analcime framework. While Na^+ preferentially adsorbs at the center of the 8-member ring, DFT calculations show that larger ions, such as Cs^+, occupy the center of the cage due to steric constraints. The computed exchange energies indicate that exchange of Na^+ by Cs^+ is thermodynamically favorable. Migration energy barriers, determined using the climbing image nudged elastic band method, show that Na^+ is mobile in analcime, diffusing through both 6-member rings and 8-member rings, with a low migration energy of about 0.3 eV; Cs^+ diffusion primarily occurs through the 8-member ring pathway, with a high energy barrier of 1.35 eV, whereas the 6-member ring pathway presents even significantly higher barriers (~3.37 eV), making it less accessible. These findings suggest that Cs^+/Na^+ exchange in analcime is thermodynamically feasible but kinetically hindered. Our work provides a theoretical foundation for the application of analcime in nuclear waste management and highlights the need for further experimental validation.

1. Introduction

With the continuous growth of global energy demand, nuclear energy has become an essential component of the energy strategies of many countries due to its high efficiency and low carbon footprint. However, the large amount of radioactive waste generated by nuclear fission reactions poses severe challenges to both the environment and human health. Among these, radioactive cesium (*e.g.*, ^{137}Cs) is particularly concerning due to its half-life of approximately 30.17 years. ^{137}Cs primarily undergoes β-decay to barium-137m (137mBa), which subsequently emits gamma radiation with an energy of approximately 662 keV.[1] Due to its high solubility and potential for bioaccumulation, ^{137}Cs is a critical issue in nuclear waste management. Once released into the environment, ^{137}Cs can enter the human body through the food chain, causing long-term radiation damage to biological systems, including cellular damage, genetic mutations, and an increased risk of cancer. For example, the large amounts of ^{137}Cs released during the Chernobyl and Fukushima nuclear accidents have had lasting impacts on surrounding ecosystems and posed severe health risks to local residents.[2–4] Therefore, the effective separation, recovery, and confinement of ^{137}Cs to minimize its ecological impact is one of the key challenges in the sustainable development of nuclear energy.[5]

Currently, the main methods for removing Cs^+ ions from aqueous solutions are chemical precipitation, membrane separation, and ion exchange processes. The chemical precipitation method[6] involves addition of chemical reagents to the contaminated solution to form insoluble cesium compounds; however, precise pH adjustment is required to ensure the effectiveness of the precipitation reaction. The generation of a large amount of Cs-containing sludge through salt precipitation significantly increases the difficulty of incorporation into an immobilizing matrix, such as cementitious or glass materials. The membrane separation method[7] utilizes the selective permeability of semipermeable membranes to separate Cs^+ ions from the solution. Common membrane technologies include reverse osmosis, nanofiltration, and electrodialysis. While these methods demonstrate good efficiency in removing radioactive ^{137}Cs, they have high equipment and operating costs, and the membranes are susceptible to contamination, requiring regular maintenance.[8] The ion exchange method employs ion-exchange materials to exchange Cs^+ ions in solution with ions on a solid matrix, thereby achieving removal.

[a] *Department of Materials Science and Engineering, University of Florida, Gainesville FL 32611, USA. E-mail: phillpot@ufl.edu*
[b] *Laboratoire Lorrain de Chimie Moléculaire L2CM, Université de Lorraine, CNRS, F-54000 Nancy, France*
[c] *Center for Hierarchical Waste Form Materials and Department of Chemistry and Biochemistry, University of South Carolina, Columbia, South Carolina 29208, USA*
† Current Address: Sandia National Laboratories, Livermore, CA, 94551, USA.
‡ Current Address: Los Alamos National Laboratory, Los Alamos, NM, 87545, USA.

Among these materials, zeolites[9,10]—naturally occurring aluminosilicate minerals—exhibit high selectivity for Cs^+ ions due to their well-defined porous structures and large specific surface areas. Furthermore, the chemical stability and mechanical strength of zeolites make them highly effective in practical applications, rendering them ideal candidates for treating radioactive wastewater. In the removal of Cs^+ ions from aqueous solutions, natural zeolites such as clinoptilolite have demonstrated significant adsorption capacity. Indeed, clinoptilolite[9] is widely used in radioactive wastewater treatment due to its high ion-exchange capacity and selectivity for Cs^+ ions. Additionally, synthetic zeolites such as Zeolite A4 and Rho-type zeolites[10] exhibit excellent Cs^+ removal performance in high-salinity environments. Recent studies have also employed density functional theory (DFT) calculations to uncover the cation exchange and adsorption mechanisms in zeolite materials, such as Faujasite-type structures, providing valuable insights that complement experimental observations.[11,12]

Analcime, a naturally occurring zeolite mineral, possesses a unique aluminosilicate framework that facilitates ion exchange, allowing the reversible substitution of its native cations with other ions in solution. This property has been widely investigated and applied in water treatment processes to remove undesirable ions from contaminated water sources.[13,14] Analcime's natural abundance and high availability could make it a cost-effective option compared to synthetic zeolites, which often require complex and energy-intensive manufacturing processes. Additionally, the utilization of industrial waste materials for the synthesis of analcime-based zeolites has been explored, potentially reducing production costs and contributing to environmental sustainability.[15]

Regarding the incorporation of Cs^+ in zeolite analcime, the experimental situation is somewhat complex. Kumar *et al.*[16] found that the analcime structure demonstrated negligible adsorption for Cs^+ ions at room temperature. Mallah *et al.*[17] also reported no adsorption of Cs^+ on both natural and synthetic analcime at temperatures below 100 °C but significant adsorption above 150 °C. In contrast, Liu *et al.*[18] reported that synthetic analcime prepared from fly ash exhibited a maximum Cs^+ adsorption capacity of 121.11 mg g^{-1} at pH = 6 and T = 25 °C, with the adsorption behavior well described by the Langmuir isotherm and a pseudo-second-order kinetic model.

Compared to other zeolites, analcime exhibits a more complex and denser framework, and its intricate crystallography poses significant challenges for understanding the adsorption and ion-exchange mechanisms of Cs^+ and other heavy metal ions. To date, only the adsorption sites of common alkali metal ions, such as Na^+, in analcime have been reported.[19] For larger ions like Cs^+, both their adsorption sites and diffusion mechanisms within the analcime framework remain poorly understood. In this work, we employ the density functional theory (DFT) method to characterize the ion-exchange and diffusion mechanisms of Cs^+ and other alkali metal ions in zeolite analcime. Computational modeling enables atomic-level manipulation at specific sites, making it particularly suitable for studying materials with complex crystallography such as analcime.[20] Through this computational study, we aim to establish a generalized model of ion exchange in analcime, providing a theoretical foundation for its practical applications.

2. Methods and crystallography

2.1. Methods

All density functional theory (DFT)[21] calculations in this work have been performed using the Vienna *Ab initio* Simulation Package (VASP).[22] The electronic self-consistency convergence criterion is set to 10^{-7} eV, ensuring high accuracy in the total energy convergence. For structural relaxation, the force convergence criterion is set to 10^{-3} eV Å. These stringent convergence criteria ensure highly precise results.

Electron states are simulated using the generalized gradient approximation (GGA) algorithm[23] with the Perdew–Burke–Ernzerhof (PBE)[23] exchange–correlation functional, which is widely used due to its balance between computational efficiency and accuracy in describing structural, electronic, and energetic properties of materials. The projector augmented wave (PAW) method[24] is employed to accurately account for the electron–ion interactions while efficiently handling the valence–core separation. In this approach, the frozen–core approximation is applied, meaning that only valence electrons are explicitly treated in the calculations, while core electrons are represented by an effective potential. To ensure numerical stability and accuracy, a plane-wave basis set with an energy cutoff of 520 eV is employed, 1.3 times the highest ENMAX value among the elements in the system (400 eV for O). The valence electron configurations considered for each element are as follows: Al ($3s^23p^1$), O ($2s^22p^4$), Si ($3s^23p^2$), Li ($1s^22s^12p^0$), Na ($2p^63s^1$), K ($3s^23p^64s^1$). Rb ($4s^24p^65s^1$) and Cs ($5s^25p^66s^1$). These valence states were selected based on the standard PAW potentials provided in VASP to ensure accurate representation of the chemical bonding and the electronic structure. We include dispersion corrections using the DFT-D2 method of Grimme.[25] While the dominant interaction between Cs^+ and the zeolite framework is electrostatic, the DFT-D2 scheme provides an improved description of additional long-range dispersion contributions that are not fully captured by conventional GGA functionals.

A 1 × 1 × 1 Monkhorst–Pack k-point grid is chosen for Brillouin zone sampling, considering the large cubic unit cell of analcime with lattice parameters $a = b = c$ = 13.567 Å. Given the relatively large unit cell size, the reciprocal space is correspondingly small, making a single Γ-point sampling (1 × 1 × 1) sufficient for accurate total energy calculations. This choice ensures computational efficiency while maintaining reliable accuracy for structural relaxation and energy evaluations.

The climbing image nudged elastic band (CI-NEB) method[26] is adopted to calculate the migration energy of extra-framework cations by interpolating multiple intermediate images between two equilibrium states. The CI-NEB approach is a widely used method for finding minimum energy pathways (MEP) in atomic diffusion and transition state calculations. Unlike the standard nudged elastic band (NEB) method,[27] CI-NEB ensures that the highest-energy image along the path precisely converges to the

true saddle point, thereby improving the accuracy of activation energy predictions. In our calculations, a spring constant of –5.0 eV Å^{-2} is used, which provides a balanced constraint on image spacing without overly distorting the energy landscape. Depending on the complexity of the migration pathway, the number of images is chosen to be either 11 or 15.

To better represent the aqueous environment's influence on the exchange behavior of extra-framework ions, an explicit solvation model is applied exclusively to aqueous cations that are involved in the ion exchange, while the analcime framework and its extra-framework cations are maintained under vacuum conditions. The specific rationale behind this modeling strategy is given in a subsequent section.

2.2. Structure of analcime zeolite

The silicious analcime (ANA) framework, shown in Fig. 1(a), is classified under the *I*3*ad* space group (#230),[19] with the chemical formula $Si_{48}O_{96}$ and lattice parameter $a = b = c =$ 13.567 Å. When Al substitutes for some of the Si, the framework is negatively charged. To compensate for this, extra-framework alkali Na^+ cations are present in the pores of the framework, presumably near the Al; the number of Na cations and Al atoms are equal to maintain the charge neutrality of the entire zeolite system. A typical composition is $Na_{16}Al_{16}Si_{32}O_{96}$.

Fig. 1(b) shows the negatively charged $Al_{16}Si_{32}O_{96}$ analcime structure with the randomly distributed Al substitutions shown in green. The model construction and Al site preference follow a theoretical study by Takaishi[28] as there is currently no experimental data on the distribution of Al. Therefore, this particular composition illustrates the structure under Al substitution rather than claiming to be a specific physical structure. Fig. 1(c) shows the same structure with the charge-compensating extra-framework Na^+ ions shown in representative position. In this work, to simplify the visualization of extra-framework cations sites and diffusion behavior, the oxygen ions are not shown. Thus, Fig. 1(d) only shows the 48 Si ions in the purely silicious unit cell, with the understanding that there is an oxygen atom between connected Si. All calculations in our work were performed in a simple analcime system with only one Al and one Na ion.

The cubic ANA framework is built from periodic units called cages, as shown in Fig. 2. A single unit cell includes 16 cages with different orientations, where only 2 cages are entirely within a single unit cell, as shown in Fig. 2(a). Other cages span unit cell boundaries, shared by two or more cells. A single cage is delineated by three highly distorted 8-member rings (rings containing eight Si atoms) and two highly distorted 6-member rings. The positions of the three

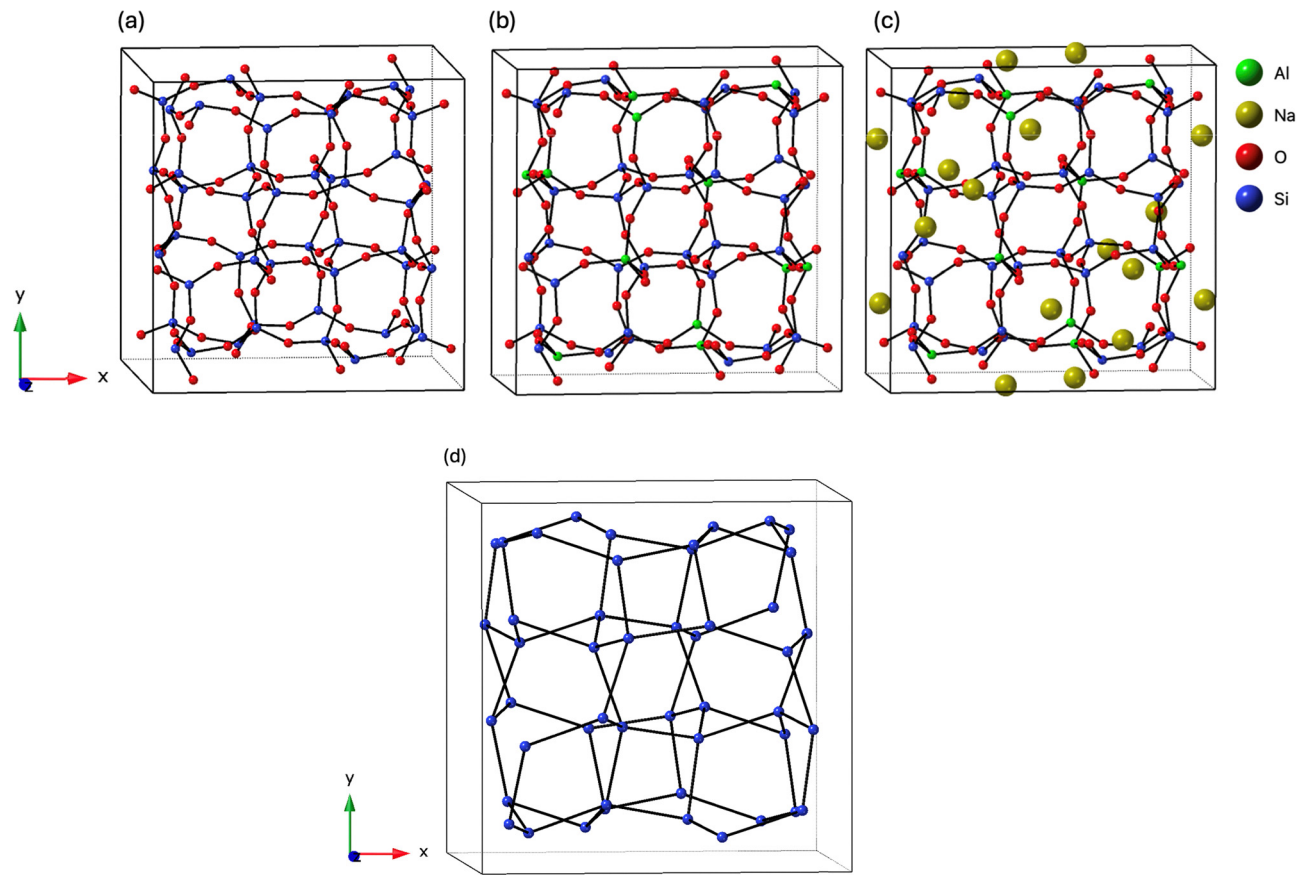

Fig. 1 (a) Structure of $Si_{48}O_{96}$, (b) structure of $Al_{16}Si_{16}O_{96}$, (c) structure of $Na_{16}Al_{16}Si_{16}O_{96}$, (d) purely silicious structure of $Si_{48}O_{96}$, with only the Si atoms shown.

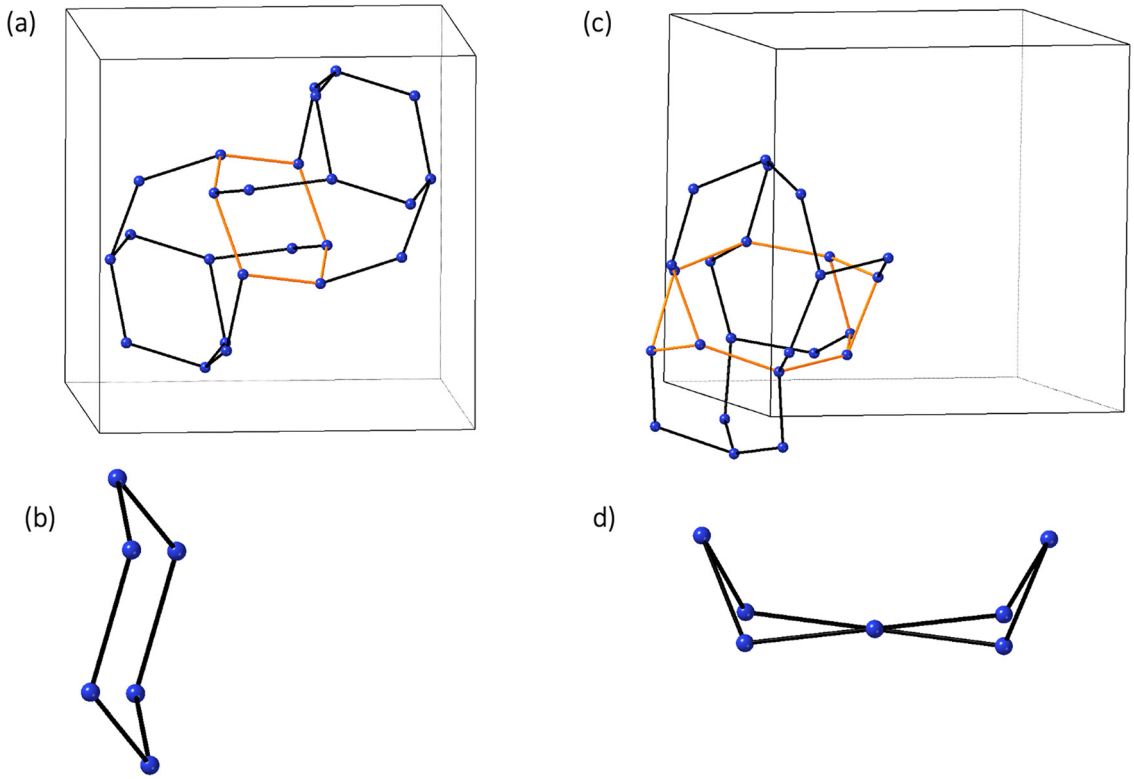

Fig. 2 (a) Two complete cages in a unit cell, connected by a six-member ring (orange), (b) a 6-member ring, (c) two cages, connected by an 8-member ring, at the left side shared by neighbor unit cells, (d) an 8-member ring.

8-member rings and two 6-member rings in the cage are marked in Fig. 2(b) and (c) respectively, from which it can be seen that these five rings are interconnected. As a result, each Si belongs to multiple different rings. We anticipate that these rings may serve as channels for the diffusion of extra-framework cations through the structure. Finally, Fig. 3 shows each of the 8-member and 6-member rings in a single cage.

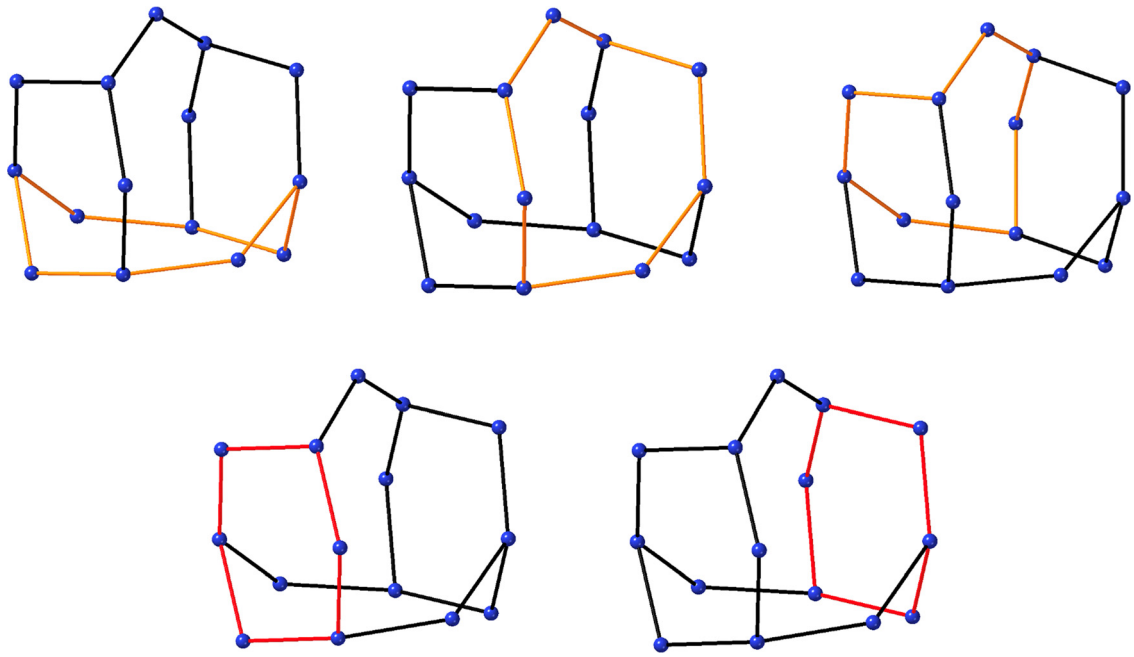

Fig. 3 Positions of three 8-member rings (orange) and two 6-member rings (red) in a single cage.

3. The energetics associated with ion exchange

In the context of ion exchange, in this section we address the question of the locations of Na^+ and Cs^+ extra-framework alkali cations in the structure, In earlier papers, the center of the 8-member ring was identified as the site for Na^+;[19,29,30] we confirm that result here and find the same location for Li^+ ions. However, we find that larger radius ions, K^+, Rb^+ and Cs^+, prefer sites different from Na^+.

The distorted structure of the 8-member rings and the different connectivities of the various atoms to other 6- and 8-member rings means that not all Si sites are structurally equivalent. Fig. 4 categorizes the Si sites into crystallographically distinct types: A (two Si atoms), B (two Si atoms) and C (four Si atoms). The center of the distorted 8-member-ring is at the middle point between B1 and B2, as shown in Fig. 4. The distance between the B1 and B2 atoms is a convenient measure of the size of the ring, 6.202 Å. Although natural and synthesized analcime compositions contain multiple Al atoms and Na^+ ions, in this study, we focus on the low-concentration limit by modeling a single Al atom and charge-compensating Na^+ ion within the relatively large unit cell. This approach allows us to isolate and capture the essential features of local Al–Na interactions while minimizing the influence of longer-range electrostatic interactions among multiple Al atoms and extra-framework cations. As such, it provides a strong baseline in which to analyze the structural and energetic behavior associated with individual ring environments.

We have determined the structure and relative energies ΔE_{rel} of Na^+ for each of these possible Al positions with respect to the energetically most favorable Al site.[31]

The Na^+ ion shifts from the center of the ring towards the Al^{3+} site due to the weaker repulsion of Na^+ by Al^{3+} than by Si^{4+}. Fig. 5 shows how the Na^+ site changes with Al positions. For the A site, Fig. 5a, the Na^+ ion is lifted out of the center of the ring

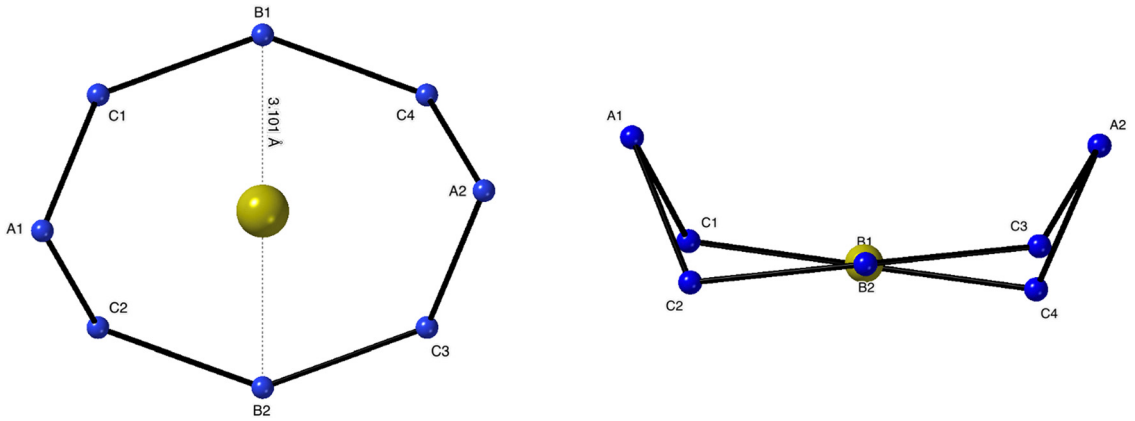

Fig. 4 Three distinct Al substitution sites and the Na^+ reference adsorption site at the center of the ring.

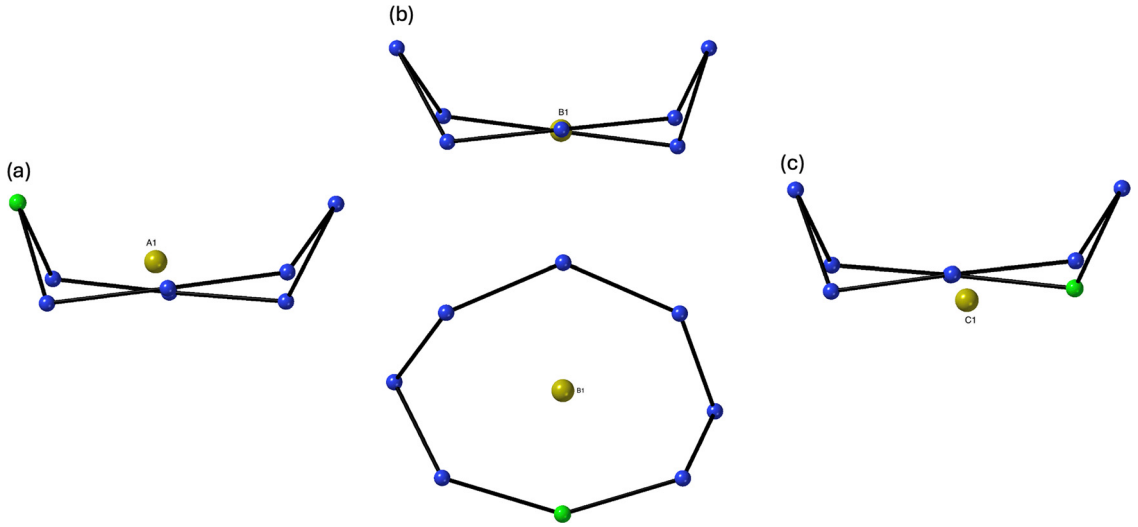

Fig. 5 Position of the Na^+ ion with respect to the position of the Al atom in the ring. The three symmetrically distintct configurations are shown: (a) Na^+ position when Al at site A1, (b) Na^+ position when Al at site B1, and (c) Na^+ position when Al at site C1.

and is attracted to the Al. When Al is in the B site, Fig. 5b, the Na^+ sits at the ring center. For the C sites, Fig. 5c, the Na^+ is again lifted out of the center of the ring. Depending on the specific position of the four C sites, Na^+ can be dragged by Al below or above the ring.

The energetic stability of the Na^+ is also influenced by Al position, as shown in Fig. 6, which presents relative energies ΔE_{rel} of Na^+ with respect to the energetically most favorable Al site.

Al on the C site is the most energetically favorable location, though the Gibbs free energy of the B site is less favorable by only 0.01 eV. The free energy of Na^+ in the presence of Al on an A site is $\sim$0.18 eV less favorable than on a C site.

Li ions follow a similar order of energies, the details of which are included in the SI.

Larger cations, K^+, Rb^+, and Cs^+, with atomic radii of 1.52 Å, 1.66 Å, and 1.81 Å respectively, are too big to sit on or close to the center of the 8-member rings. Rather, they occupy sites in the interior of the cage, as shown in Fig. 7(a). To characterize their positions, it is useful to identify the cage center. The centers of three 8-member rings, marked by three semi-transparent black spheres in Fig. 7(b), form an equilateral triangle, with sides of 4.154 Å in length. The center of the cage can reasonably be defined to be the center of the triangle, as shown in Fig. 7(b).

As in the case of Na^+, different Al positions result in these larger alkali cations taking positions different from the reference center. Fig. 8(a) shows three types of Al substitution sites based on the topology of the cage. However, the symmetry of the sites with respect to the cage is different from that with respect to an eight-member ring. First, the four C sites in the 8-member ring are split into two different sites with respect to the cage: as Fig. 8(b) shows, type I corresponds to C2 and C4 sites in the 8-member ring, which are below the plane of the ring, while type II corresponds to C1 and C3 sites in the 8-member ring, which are above the plane of the ring. The A and B sites, inequivalent with respect to the symmetry of the ring, are equivalent to each other with regards to the cage and are designated type III.

The relative energies ΔE_{rel} of Cs^+ for all three Al positions is shown in Fig. 9. Al on the III cite leads to the most energetically stable site.

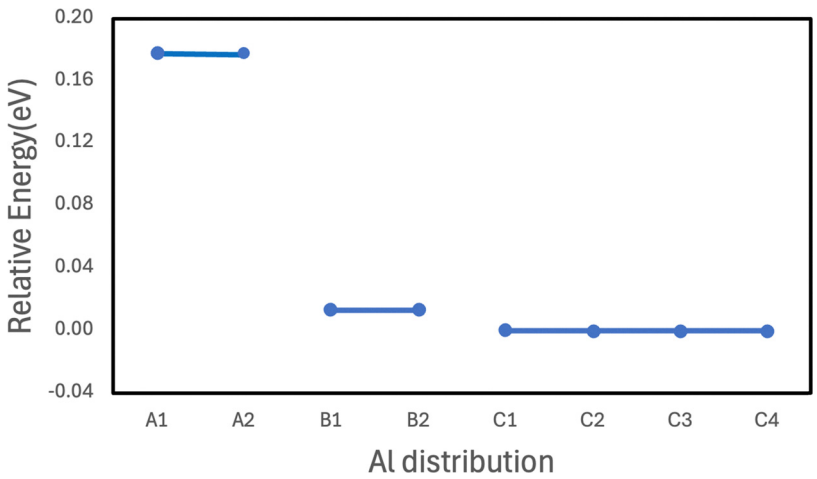

Fig. 6 Na^+ relative energies ΔE_{rel} as a function of the Al position.

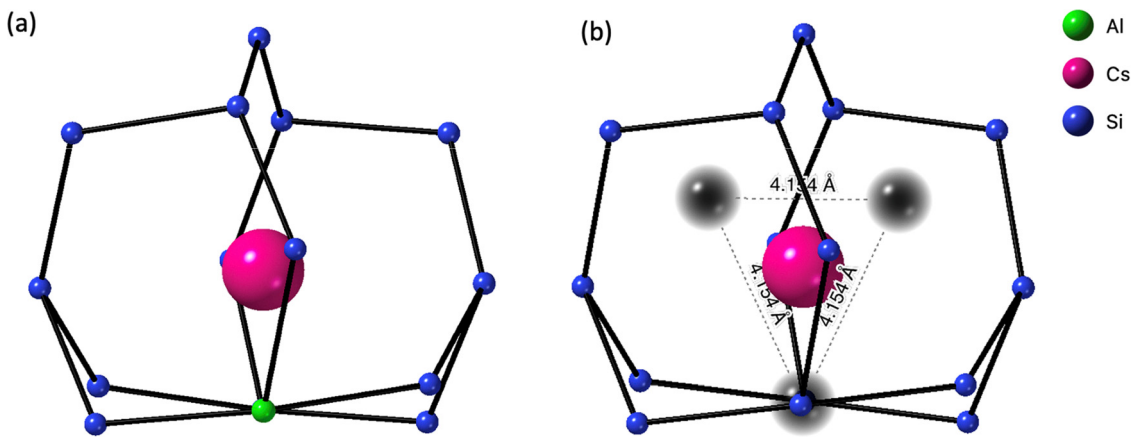

Fig. 7 (a) Cs^+ adsorption site at the center of the cage. (b) Definition of the cage center.

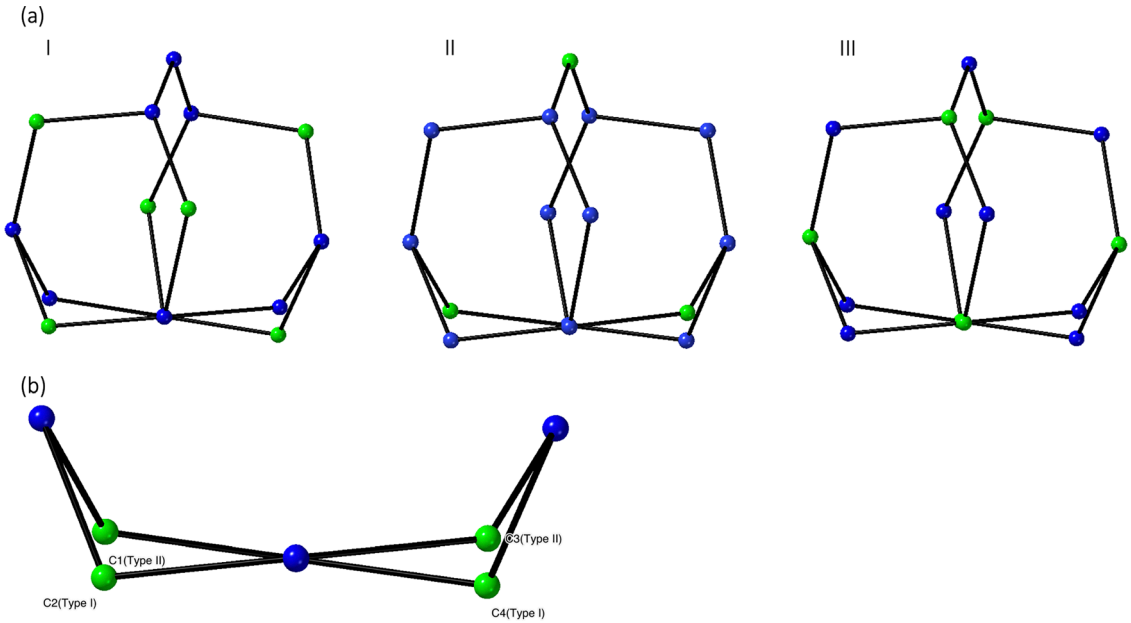

Fig. 8 (a) Three types of Al substitution sites, I, II, and III, relative to cage center, (b) C sites with respect to 8-member rings split into type I and type II with respect to cages.

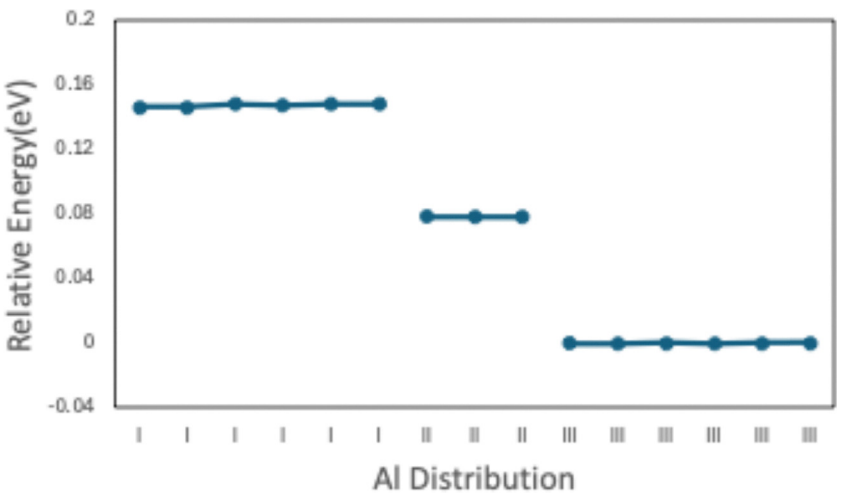

Fig. 9 Cs^+ relative energies ΔE_{rel} as a function of Al position.

While these site-specific interactions provide critical insight into local energetic preferences, a complete thermodynamic understanding of Cs^+ incorporation requires assessing the exchange energy between Cs^+ and Na^+ ions. The exchange energy of Cs^+ with Na^+ in analcime is calculated from the difference in the incorporation energies:[11,12]

$$E_{ex} = E_{CsAlANA} + E_{Na.(H_2O)_4^+} + 6E_{H_2O} - \left(E_{NaAlANA^-} + E_{Cs.(H_2O)_{10}^+}\right)$$

where the reference state of Na^+ and Cs^+ ions is hydrated and that of analcime is dehydrated. This approach is justified based on the fact that, in aqueous environments such as those encountered in experimental ion exchange systems, external ions typically exist as hydrated species. Their hydration shells significantly contribute to the thermodynamics of the overall process. The analcime framework was modeled in a dehydrated state. This simplification is justified by the observation that the presence or absence of water molecules within the zeolite pores should have a relatively minor influence on the overall ion exchange energies, since their hydration is not likely to depend on whether the extra-framework ions are Na^+ or Cs^+. Moreover, analcime has a relatively small and constrained cage structure. Our DFT simulations confirm that each cage is capable of accommodating only one species—either a water molecule or a Cs^+ ion, and the preferred location for a water molecule inside the cage overlaps with that of Cs^+, as shown in Fig. 10.

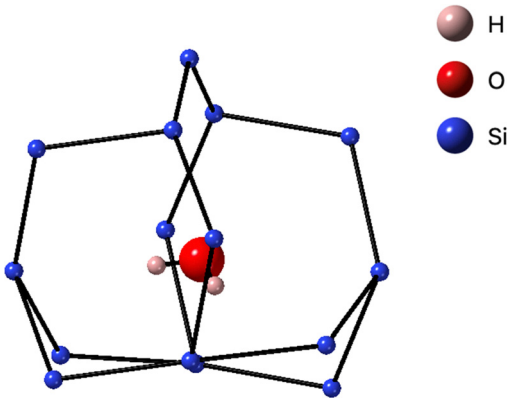

Fig. 10 Water molecule adsorption site at the center of the cage.

Consequently, once a Cs^+ ion is incorporated into the framework, there is no available space for the co-adsorption of a water molecule within the same cage.

In constructing the reference state for pure water, we considered configurations ranging from one to seventeen water molecules placed in a disorderly way in an 8 × 8 × 8 Å vacuum box. The density reaches 1 g cm^{-3} when there are seventeen water molecules in the box. As shown in Fig. 11, the total energy of the system scales linearly with the number of water molecules, indicating minimal intermolecular interactions under these conditions. Therefore, we adopted the slope, −14.85 eV, as the reference energy for a water molecule in liquid state.

In this study, the Na^+ is hydrated by 4 water molecules in a 20 × 20 × 20 Å vacuum box. This degree of hydration is based on experimental characterization.[32,33] The Cs^+ is hydrated by 10 water molecules[34] in a 20 × 20 × 20 Å vacuum box. Rb^+ and K^+ also follow a similar order of energies, details of which are included in the SI.

As Table 1 shows, the exchange energy ranges from −1.74 eV to −1.41 eV depending on the Al position. These negative values indicate that the exchange of Cs^+ for Na^+ is energetically favorable at all sites. When Al is at the A site in the 8-member ring and at the type II site in the cavity, the exchange process will be the most favorable. More information on the reference state and the various energy contributions to the exchange calculation are included in the SI.

Table 1 Exchange energy when Al is at different sites

Al position		Exchange energy (eV)
CsAlANA(I)	NaAlANA(C)	−1.41
CsAlANA(II)	NaAlANA(C)	−1.48
CsAlANA(III)	NaAlANA(A)	−1.74
CsAlANA(III)	NaAlANA(B)	−1.57

In summary, these results provide a thermodynamic assessment of alkali ion exchange in analcime, focusing on the exchange process of Na^+ by Cs^+. We confirmed that smaller alkali ions Na^+ and Li^+ preferentially occupy the center of 8-member rings, while larger ions like Cs^+, Rb^+, and K^+ tend to reside near the center of the cage due to steric constraints. Through hydration-referenced exchange energy analysis, we demonstrated that Cs^+ exchange with Na^+ is energetically favorable across all tested configurations.

4. Diffusion behavior of extra-framework alkali cations

Ion exchange for sequestration involves the replacement of Na^+ ions by Cs^+ ions. In the previous section, we have seen that this is thermodynamically favorable. However, for it to be a viable process, it also needs to be kinetically possible. Therefore, in this section we characterize the diffusive behavior of Na^+ and Cs^+ ions through the analcime framework.

For small radii cations, Li^+ and Na^+, either 8-member-ring and 6-member-ring channels are large enough to diffuse through. A Na^+ ion can migrate from one adsorption site (close to the center of an 8-member ring) to the neighboring equivalent adsorption site through the center of 6-member ring. Fig. 12(a) shows the diffusion path and the associated energy

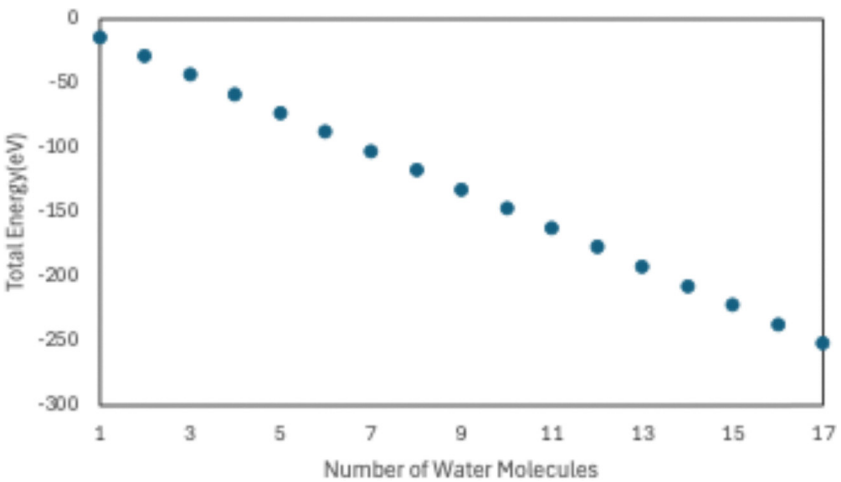

Fig. 11 Total energy of systems containing different numbers of water molecules (1–17) in a 20 × 20 × 20 Å vacuum box.

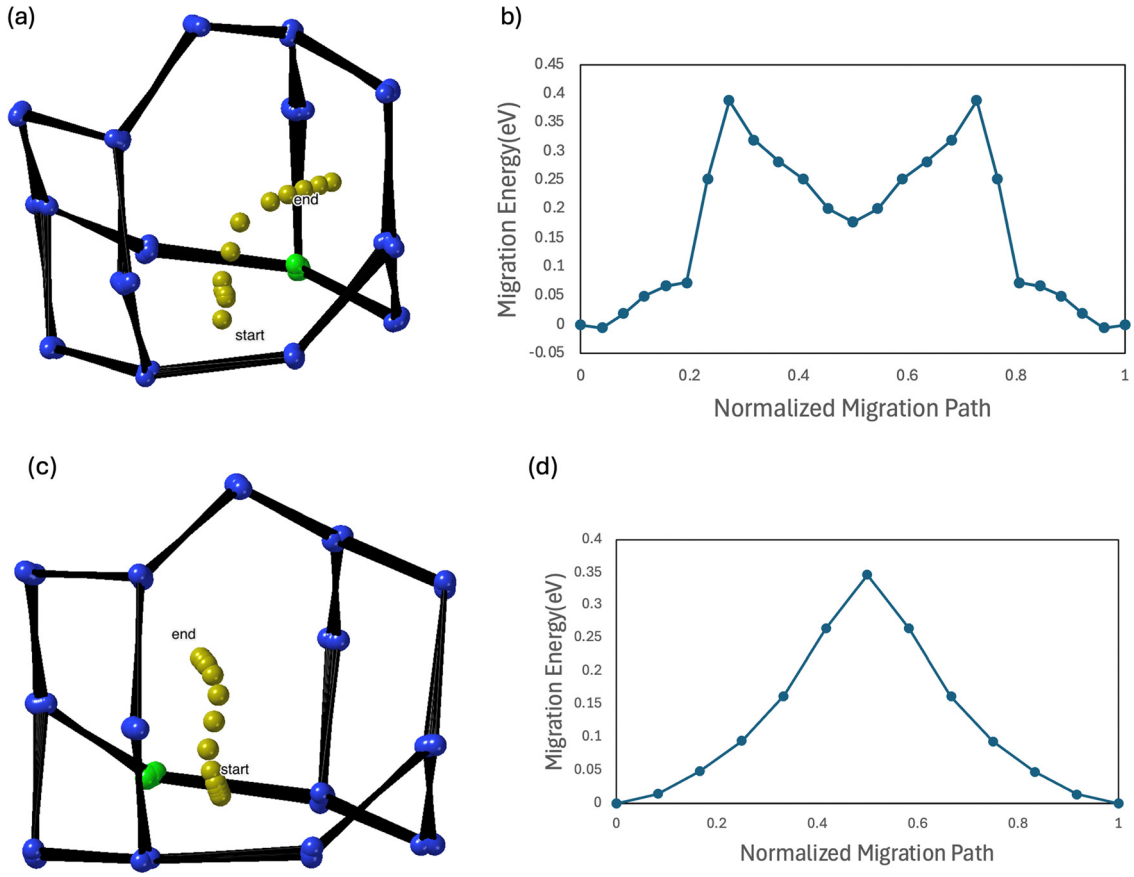

Fig. 12 Migration energy profile for Na^+. (a) The upper part illustrates migration from an 8-member ring to the neighboring 6-member ring and (b) the corresponding migration energy profiles. (c) The lower part illustrates migration from an 8-member ring to the neighboring 8-member ring and (d) the corresponding migration energy profile.

profile as determined from CI-NEB calculations. The path shown is from the adsorption site to the peak of the barrier, which lies at the center of the 6-member ring. Fig. 12(b) shows the energy along the diffusion path with a barrier height

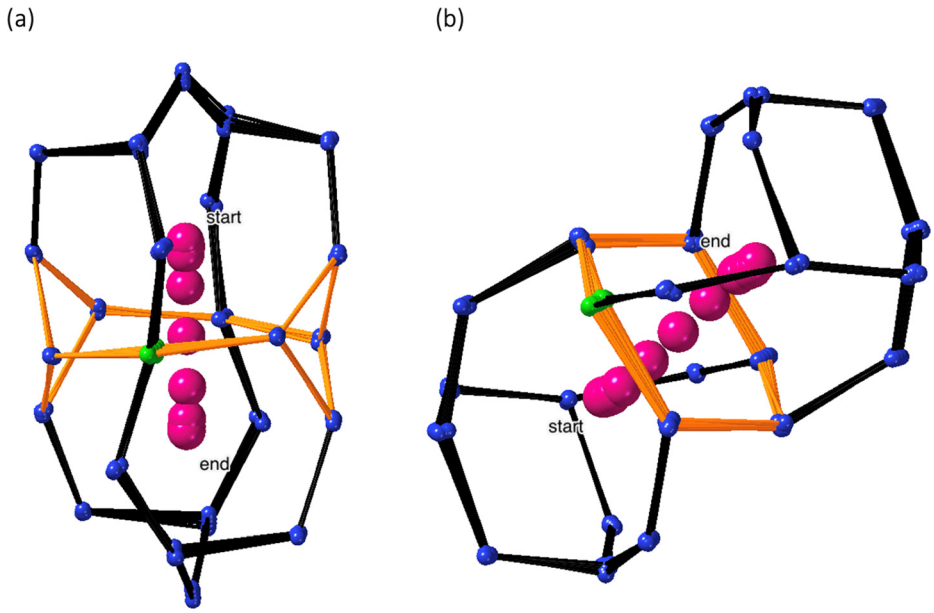

Fig. 13 Two migration paths for Cs^+ *via*, (a) 8-member ring channel, (b) 6-member-ring channel.

of 0.39 eV. Interestingly, there is not a single peak at the center of the 6-member rings, but rather two peaks, each very close to the center of the two cages. Just as the Al position affects the adsorption energy itself, the Al position has a small effect on the energy barrier, as shown in the additional migration energy profiles in the SI.

The migration path of Na^+ ions though the 8-member rings is simpler, as shown in Fig. 12(c), also showing a maximum close to the center of the cage. The height of the corresponding barrier, Fig. 12(d), is 0.35 eV, similar to the migration energy for the 6-member ring channel as the two migration paths have the same peak position.

The story is somewhat different for K^+, Rb^+ and Cs^+. Their adsorption sites are close to the center of the cage, and so must pass through unfavorable sites at the centers of the 6- or 8-member rings during migration, as shown in Fig. 13.

The first pathway starts from the adsorption site at the cage center, travels through the center of the 8-member ring and ends up at the neighboring cage center. The migration energy profile when Al is at site II, shared by two cages, is shown in Fig. 14. The saddle point is at the center of the 8-member ring. *i.e.*, at the Na^+ adsorption site. The migration energy for Cs^+ is 1.35 eV, with lower energies 0.75 eV and 0.49 eV for the smaller Rb^+ and yet smaller K^+ ions. The migration energy varies slightly with Al positions, leading to a nonsymmetric migration energy profile, as shown in the SI.

The second pathway starts from the cage center, travelling through the center of the 6-member rings, ending up at the neighboring cage center. The migration energy profile is shown in Fig. 15. Unlike the 8-member ring migration path, the 6-member ring paths are equivalent when Al is at any of 6 sites of the 6-member ring. The saddle point is near the center of the 6-member ring, though the exact position depends on the species. Due to the smaller size of the 6-member ring channel compared to the 8-member ring channel, the energy barrier for Cs^+ increases to 3.37 eV. Such a high energy barrier indicates that Cs^+ cannot diffuse through 6-member-ring channels. The barriers for Rb^+ and K^+ are smaller, 1.62 eV for Rb^+ and 0.77 eV for K^+, but still substantially larger than through the 8-member ring. Thus, for all three cations, migration through 8-member rings should dominate the diffusion if diffusion occurs under a given condition. Importantly, the 8-member rings form a continuous, interconnected network throughout the analcime framework, allowing for long-range ion transport. As a result, the poor accessibility of the 6-member ring channels does not significantly impede overall cation mobility within the structure.

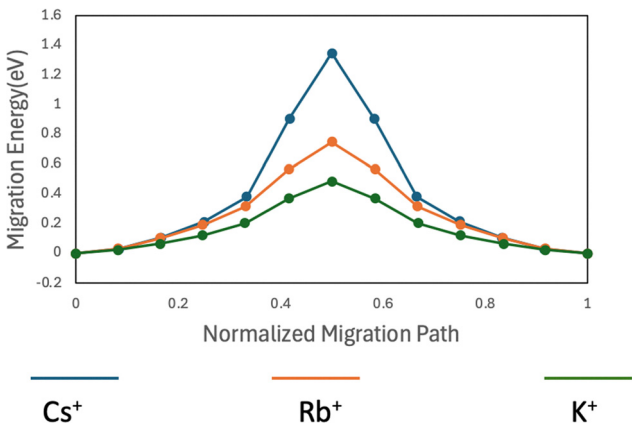

Fig. 14 Migration energy profile of the 8-member ring channel path for Cs^+, Rb^+, and K^+.

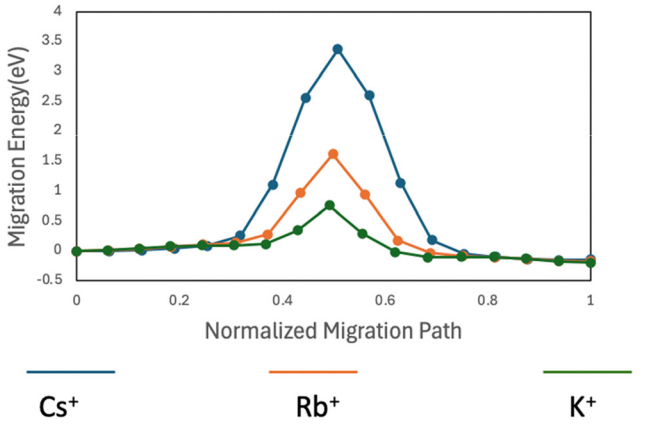

Fig. 15 Migration energy profile of 6-member ring channel paths for Cs^+, Rb^+, and K^+.

The calculated 8-member ring migration barrier of 1.35 eV for Cs^+ in analcime raises the question of whether such a value is prohibitively high for diffusion to occur. A direct assessment of diffusivity is complicated by the lack of reliable estimates for the diffusion pre-factor (D_0), making it difficult to evaluate migration rates solely from the energy barrier. Nonetheless, comparison with experimental observations provides useful insights. Na^+, which is commonly found in both natural and synthetic analcime, has a reported migration barrier of approximately 0.3 eV, consistent with facile mobility at ambient conditions. In contrast, Cs^+ is not appreciably absorbed by analcime at room temperature, and measurable adsorption is only observed at elevated temperatures above 150 °C.[16,17] The 1.35 eV barrier for Cs^+ is roughly four times larger than that of Na^+, and according to the Arrhenius relation, the exponential factor $\exp(-E_a/RT)$ for Na^+ is about 16 orders of magnitude higher than for Cs^+ at a given temperature. This analysis indicates that Cs^+ migration in analcime requires substantially higher thermal activation.

5. Conclusions

In this work, we have systematically investigated the incorporation and diffusion behavior of Cs^+ in analcime using DFT calculations. Our results reveal that, unlike Na^+, which preferentially adsorbs at the center of the 8-member ring, Cs^+ tends to occupy the center of the cage due to its larger ionic radius. The calculated exchange energies indicate that Cs^+ incorporation into analcime is thermodynamically favorable.

Furthermore, calculations of energy barriers to migration demonstrate that Na^+ exhibits low activation energies ($\sim$0.35 eV)

for migration through both 6-member and 8-member ring channels, consistent with the fact that Na^+ is typically observed in natural analcime. By contrast, Cs^+ primarily migrates through the 8-member ring pathway with an energy barrier of 1.35 eV, while diffusion through the 6-member ring is significantly hindered by a much higher energy barrier of 3.37 eV. The larger radius of Cs^+ makes it less mobile than Na^+, which suggests that higher thermal activation is required to enable Cs^+ diffusion, consistent with the experimental findings by Kumar and Mallah *et al.* described in the introduction.

The complete Cs^+ exchange mechanism can be summarized as the following: once a Cs^+ ion enters the cage center, it disturbs the charge balance of the analcime system due to the excess positive charge. Given that Cs^+ replacing Na^+ is energetically favorable, the system can be expected to expel the Na^+ to restore charge neutrality.

Overall, our study provides a theoretical foundation for understanding alkali ion exchange in the zeolite analcime. Further experimental and theoretical studies are necessary to validate these findings and explore potential modifications to enhance Cs^+ incorporation in analcime. Future research could investigate the role of water coordination, the effect of framework flexibility.

Conflicts of interest

There are no conflicts to declare.

Data availability

All data supporting the findings of this study are available within the main article and the supplementary information (SI). The supplementary information contains additional analysis of the analcime framework structure to aid interpretation, the raw DFT data (total energies and the reference states for water and the relevant ions) and illustration of different migration path and migration profiles when Al at different sites. See DOI: **https://doi.org/10.1039/d5cp02373d**.

The raw DFT input/output files and NEB calculation data used to evaluate migration energy barriers are available from the corresponding author upon reasonable request.

Acknowledgements

We gratefully acknowledge Agnès Grandjean for very useful discussions. This work was supported by the Center for Hierarchical Waste Form Materials (CHWM), an Energy Frontier Research Center (EFRC) funded by the United States Department of Energy Office of Basic Energy Sciences through the Award DESC0016574. We acknowledge University of Florida Research Computing for providing computational resources and support that have contributed to the research results reported in this publication.

References

1 J. G. V. Taylor and J. S. Merritt, Decay of Cesium-137 Determined by Absolute Counting Methods, *Anal. Chem.*, 1965, **37**, 351–354, DOI: **10.1021/ac60224a011**.
2 M. Orita, K. Nakashima, N. Hayashida, Y. Endo, S. Yamashita and N. Takamura, Concentrations of Radiocesium in Local Foods Collected in Kawauchi Village after the Accident at the Fukushima Dai-ichi Nuclear Power Station, *Sci. Rep.*, 2016, **6**, 28470, DOI: **10.1038/srep28470**.
3 K.-M. Wai, D. Krstic, D. Nikezic, T.-H. Lin and P. K. N. Yu, External Cesium-137 Doses to Humans from Soil Influenced by the Fukushima and Chernobyl Nuclear Power Plants Accidents: A Comparative Study, *Sci. Rep.*, 2020, **10**, 7902, DOI: **10.1038/s41598-020-64812-9**.
4 T. J. Yasunari, A. Stohl, R. S. Hayano, J. F. Burkhart, S. Eckhardt and T. Yasunari, Cesium-137 Deposition and Contamination of Japanese Soils due to the Fukushima Nuclear Accident, *Proc. Natl. Acad. Sci. U. S. A.*, 2011, **108**, 19530–19534, DOI: **10.1073/pnas.1112058108**.
5 H.-C. Zur Loye, T. Besmann, J. Amoroso, K. Brinkman, A. Grandjean, C. H. Henager, S. Hu, S. T. Misture, S. R. Phillpot, N. B. Shustova, H. Wang, R. J. Koch, G. Morrison and E. Dolgopolova, Hierarchical Materials as Tailored Nuclear Waste Forms: A Perspective, *Chem. Mater.*, 2018, **30**, 4475–4488, DOI: **10.1021/acs.chemmater.8b00766**.
6 Y. Cao, L. Zhou, H. Ren and H. Zou, Determination, Separation and Application of ^{137}Cs: A Review. Int. J. Environ, *Res. Public Health*, 2022, **19**, 10183, DOI: **10.3390/ijerph191610183**.
7 S. Zhuang and J. Wang, Cesium Removal from Radioactive Wastewater by Adsorption and Membrane Technology, *Front. Environ. Sci. Eng.*, 2024, **18**, 38, DOI: **10.1007/s11783-024-1798-1**.
8 M. Jafari, M. Vanoppen, J. M. C. van Agtmaal, E. R. Cornelissen, J. S. Vrouwenvelder, A. Verliefde, M. C. M. van Loosdrecht and C. Picioreanu, Cost of Fouling in Full-Scale Reverse Osmosis and Nanofiltration Installations in the Netherlands, *Desalination*, 2021, **500**, 114865, DOI: **10.1016/j.desal.2020.114865**.
9 H. Y. Chung, H. S. Kim, H.-K. Jeong, M. Park, D.-Y. Chung, K.-Y. Lee, E.-H. Lee and W. T. Lim, Selective Removal of Radioactive Cesium from Nuclear Waste by Zeolites: On the Origin of Cesium Selectivity Revealed by Systematic Crystallographic Studies, *J. Phys. Chem. C*, 2017, **121**, 10594–10608, DOI: **10.1021/acs.jpcc.7b02432**.
10 M. Jiménez-Reyes, P. T. Almazán-Sánchez and M. Solache-Ríos, Radioactive Waste Treatments by Using Zeolites: A Short Review, *J. Environ. Radioact.*, 2021, **233**, 106610, DOI: **10.1016/j.jenvrad.2021.106610**.
11 L. Sellaoui, E. P. Hessou, M. Badawi, M. S. Netto, G. L. Dotto, L. F. O. Silva, F. Tielens, J. Ifthikar, A. Bonilla-Petriciolet and Z. Chen, Trapping of Ag^+, Cu^{2+}, and Co^{2+} by Faujasite Zeolite Y: New Interpretations of the Adsorption Mechanism via DFT and Statistical Modeling Investigation, *Chem. Eng. J.*, 2021, **420**, 127712, DOI: **10.1016/j.cej.2020.127712**.

12 A. T. Ta, A. Daouli, R. S. Ullberg, E. Fonseca, V. Proust, A. Grandjean, R. G. Hennig, H.-C. zur Loye, M. Badawi and S. R. Phillpot, Incorporating Solvent Effects in DFT: Insights from Cation Exchange in Faujasites, *Phys. Chem. Chem. Phys.*, 2024, **26**, 14561–14572, DOI: **10.1039/d4cp00467a**.

13 Y. Kang, B. Y. Im, J.-J. Choi, J.-H. Yoon and D.-G. Kim, Synthesis of Analcime Zeolite Using Al and Si from Waste Resources for the Removal of Pb/Cd Ions from Aqueous Solution, *Arch. Metall. Mater.*, 2022, **67**, 67–72, DOI: **10.24425/amm.2022.137473**.

14 M. Abdul-Moneim, A. A. Abdelmoneim, A. A. Geies and S. O. Farghaly, Synthesis, Characterization of Analcime and Its Application in Water Treatment from Heavy Metal. Assiut Univ. Bull, *Environ. Res.*, 2018, **21**(1), 1–22.

15 L. F. Magalhães, G. R. da Silva, A. B. Henriques, V. A. A. de Freitas and A. E. C. Peres, Synthesis of Analcime Zeolite from Glass Powder Waste and Aluminium Anodizing Waste, *Silicon*, 2024, **16**, 4173–4185, DOI: **10.1007/s12633-024-02992-z**.

16 M. M. Kumar and H. Jena, Direct Single-Step Synthesis of Phase Pure Zeolite Na–P1, Hydroxy Sodalite and Analcime from Coal Fly Ash and Assessment of Their Cs^+ and Sr^{2+} Removal Efficiencies, *Microporous Mesoporous Mater.*, 2022, **333**, 111738, DOI: **10.1016/j.micromeso.2022.111738**.

17 M. H. Mallah, H. Soorchi and T. Faghih Jooybari, Development of Empirical Equation for Analcime in the Treatment of Nuclear Waste, *Ann. Nucl. Energy*, 2012, **47**, 140–145, DOI: **10.1016/j.anucene.2012.04.015**.

18 R.-Y. Liu, L.-X. Zou, Q. Huang, X.-H. Cao and C. Yang, Synthesis of Analcime from Fly Ash and Its Adsorption of Cs^+ in Aqueous Solution, *J. Radioanal. Nucl. Chem.*, 2021, **329**, 103–113, DOI: **10.1007/s10967-021-07799-5**.

19 W. H. I. Taylor, The structure of analcite ($NaAlSi_2O_6{\cdot}H_2O$), *Z. Kristallogr. - Cryst. Mater.*, 1930, **74**, 1–19, DOI: **10.1524/zkri.1930.74.1.1**.

20 M. Khosravi, V. Murthy and I. D. R. Mackinnon, Evaluation of DFT Methods to Calculate Structure and Partial Atomic Charges for Zeolite N, *Comput. Mater. Sci.*, 2020, **171**, 109225, DOI: **10.1016/j.commatsci.2019.109225**.

21 P. Hohenberg and W. Kohn, Inhomogeneous Electron Gas, *Phys. Rev.*, 1964, **136**, B864–B871, DOI: **10.1103/PhysRev.136.B864**.

22 G. Kresse and J. Hafner, Ab Initio Molecular Dynamics for Liquid Metals, *Phys. Rev. B: Condens. Matter Mater. Phys.*, 1993, **47**, 558–561, DOI: **10.1103/PhysRevB.47.558**.

23 J. P. Perdew, K. Burke and Y. Wang, Generalized Gradient Approximation for the Exchange-Correlation Hole of a Many-Electron System, *Phys. Rev. B: Condens. Matter Mater. Phys.*, 1996, **54**, 16533–16539, DOI: **10.1103/PhysRevB.54.16533**.

24 G. Kresse and D. Joubert, From Ultrasoft Pseudopotentials to the Projector Augmented-Wave Method, *Phys. Rev. B: Condens. Matter Mater. Phys.*, 1999, **59**, 1758–1775, DOI: **10.1103/PhysRevB.59.1758**.

25 S. Grimme, Semiempirical GGA-Type Density Functional Constructed with a Long-Range Dispersion Correction, *J. Comput. Chem.*, 2006, **27**, 1787–1799, DOI: **10.1002/jcc.20495**.

26 G. Henkelman, B. P. Uberuaga and H. Jónsson, A Climbing Image Nudged Elastic Band Method for Finding Saddle Points and Minimum Energy Paths, *J. Chem. Phys.*, 2000, **113**, 9901–9904, DOI: **10.1063/1.1329672**.

27 H. Jónsson, G. Mills and K. W. Jacobsen, Nudged Elastic Band Method for Finding Minimum Energy Paths of Transitions, In *Classical and Quantum Dynamics in Condensed Phase Simulations*, ed, B. J. Berne, G. Ciccotti, D. F. Coker, World Scientific, Singapore, 1998, pp. 385–404, DOI: **10.1142/9789812839664_0016**.

28 T. Takaishi, Ordered Distribution of Al Atoms in the Framework of Analcimes, *J. Chem. Soc., Faraday Trans.*, 1998, **94**, 1507–1518, DOI: **10.1039/a708826d**.

29 F. Mazzi and E. Galli, Is Each Analcime Different?, *Am. Mineral.*, 1978, **63**, 448–460.

30 M. Kato and T. Hattori, Ordered Distribution of Aluminum Atoms in Analcime, *Phys. Chem. Miner.*, 1998, **25**, 556–565, DOI: **10.1007/s002690050148**.

31 S. Chibani, M. Chebbi, S. Lebègue, T. Bučko and M. Badawi, A DFT Investigation of the Adsorption of Iodine Compounds and Water in H-, Na-, Ag-, and Cu- Mordenite, *J. Chem. Phys.*, 2016, **144**, 244705, DOI: **10.1063/1.4954659**.

32 P. R. Smirnov and V. N. Trostin, Structure of the Nearest Surrounding of the Na^+ Ion in Aqueous Solutions of Its Salts, *Russ. J. Gen. Chem.*, 2007, **77**(5), 844–850, DOI: **10.1134/S1070363207050052**.

33 D. Z. Caralampio, J. M. Martínez, R. R. Pappalardo and E. S. Marcos, The Hydration Structure of the Heavy-Alkalines Rb^+ and Cs^+ through Molecular Dynamics and X-Ray Absorption Spectroscopy: Surface Clusters and Eccentricity, *Phys. Chem. Chem. Phys.*, 2017, **19**(42), 28993–29004, DOI: **10.1039/c7cp05346k**.

34 X. Wang, S. Pandey, M. Fullarton and S. R. Phillpot, Study of Incorporating Cesium into Copper Hexacyanoferrate by Density Functional Theory Calculations, *J. Phys. Chem. C*, 2021, **125**, 24273–24283, DOI: **10.1021/acs.jpcc.1c08702**.